

# Electrically Tunable Microlens Array Enabled by Polymer-Stabilized Smectic Hierarchical Architectures

Jin-Bing Wu, Sai-Bo Wu, Hui-Min Cao, Quan-Ming Chen, Yan-Qing Lu, and Wei Hu\*

Liquid crystals (LCs) are key functional materials that are broadly adopted in various fields due to their stimuli-responsiveness. Recently, LCs with hierarchical architectures have brought new effects to optics and attracted intensive attention. In smectic A phase, the parallel molecular layers are periodically wrapped to form toric focal conic domains (TFCDs) under antagonistic boundary conditions (i.e., hybrid alignment conditions). TFCD shows great potential in nanofabrication and integral imaging. However, the arbitrary tailoring of TFCD is still challenging, and the robustness of hierarchical configuration hinders the tunability. Here, a radial alignment lattice is adopted to guide the local orientation of LCs and thus facilitates predefining the lattice symmetry and domain size of TFCDs. By introducing polymer stabilization and optimizing the composition, the sample simultaneously maintains the director distribution inside smectic layers and possesses the stimuli-responsiveness of nematic phase at room temperature. By this means, microlens arrays are demonstrated with reversible electrical tunability. The strategy can be extended to other smectic configurations and may upgrade existing dynamic optics.

polarization selectivity and a designable frequency range. Such manipulation can be further extended to 3D by predefining the organization of double-helix blue-phase LC.<sup>[7]</sup> The complicated configuration of LCs provides a practical solution for large-scale parallel and multidimensional manipulation of light, which is of vital importance in advanced techniques, including high-capacity optical communications,<sup>[8]</sup> optical neural networks,<sup>[9]</sup> and augmented/virtual realities.<sup>[10]</sup>

In smectic A (SmA) phase, rod-like LC molecules are stacked into ordered lamellar structures with director oriented toward the normal of layer planes.<sup>[11]</sup> Under antagonistic boundary conditions, these parallel layers are periodically wrapped to form toric focal conic domains (TFCDs).<sup>[12]</sup> Such hierarchical configurations are used for fabricating superhydrophobic surfaces<sup>[13]</sup> and nanoparticle matrices.<sup>[14]</sup> Moreover, the perfect

rotational invariance of TFCD and the gradient refractive index change caused by its specific director field endow TFCDs with the function of focusing light as a microlens array (MLA).<sup>[15]</sup> The system still faces two challenges that severely hinder its practical applications. One is the free design and faithful generation of TFCD array. Many efforts have been made to improve the domain size uniformity and regulate the lattice order in recent years. 3D artificial reliefs, such as microchannels and micropillars, are adopted to geometrically confine the layer deformation and thus enhance the controllability of the ordered TFCDs.<sup>[16]</sup> Preprogrammed anchoring surfaces generated by chemical modification,<sup>[17]</sup> mechanical scrubbing,<sup>[18]</sup> and multiple-stamping<sup>[19]</sup> supply a relatively simple and efficient approach for layered superstructure tailoring. Additionally, using multidomain photoalignment, segmented and deformed TFCDs are realized.<sup>[20]</sup> Despite the above impressive progress, it remains elusive to freely define the size and location of TFCDs on the same sample. The other challenge is the strong intermolecular interactions and constant-layer-space restraint, leading the SmA to rarely respond to external stimuli and thus preventing dynamic tunability. Researchers have reported the electrically driven rotation and pitch tuning,<sup>[21]</sup> as well as light-driven rotation of oily streaks,<sup>[22]</sup> another typical smectic texture occurs at lower film thickness. Unfortunately, the above tunabilities are not supported by TFCDs. Although some attempts have been reported via keeping a certain electric field across the nematic (N) to smectic phase transition,<sup>[23]</sup> it is still challenging

## 1. Introduction

Liquid crystals (LCs) are kinds of functional materials characterized by physical anisotropy that tend to respond to various external stimuli. On the basis of this unique property, LCs are adopted as a large-scale parallel light valve in dominant LC displays.<sup>[1]</sup> Additionally, LCs can spatially and dynamically modulate the phase of light with high resolution and efficiency, which play key roles in all-optical interconnections,<sup>[2]</sup> tunable lenses,<sup>[3]</sup> and LiDAR.<sup>[4]</sup> Recently, the self-assembly feature of LCs has attracted intensive attention.<sup>[5]</sup> With the rich ordered and complicated structures, new optical effects are introduced, and advanced applications are inspired. For instance, via spatially manipulating the initial orientations of the standing helices of cholesteric LC, the Bragg–Berry phase can be arbitrarily modulated.<sup>[6]</sup> It enables a reflective phase modulation with circular

J.-B. Wu, S.-B. Wu, H.-M. Cao, Q.-M. Chen, Y.-Q. Lu, W. Hu  
National Laboratory of Solid State Microstructures  
Key Laboratory of Intelligent Optical Sensing and Manipulation  
and College of Engineering and Applied Sciences  
Nanjing University  
Nanjing 210023, P. R. China  
E-mail: huwei@nju.edu.cn

 The ORCID identification number(s) for the author(s) of this article can be found under <https://doi.org/10.1002/adom.202201015>.

DOI: 10.1002/adom.202201015

to directly modulate TFCD configurations. If one can overcome the above restrictions, new architectures with tunable optical functions can be expected.

Here, a high-precision photoalignment layer is adopted to mimic the intrinsic director distribution of the bottom layer of TFCD. The radial prealignments successfully guide the local orientation of LCs and thus correspondingly facilitate the emergence of objective TFCDs. By regulating the locations and species of alignment singularities as well as the area of alignment regions, the lattice symmetry and domain size of TFCD array are freely manipulated. After introducing polymer stabilization, the director distribution inside smectic layers is fixed even though the system transforms to N phase. This treatment endows the LC hierarchical configurations with tunability. We optimize the composition of LCs to achieve N phase at room temperature, and demonstrate a reversibly tunable focal length of the MLA as a result of the structural evolution of TFCDs driven by electric field. The strategy can be extended to other smectic hierarchical configurations and may inspire unrepresented optical structures with pronounced tunability.

## 2. Results and Discussion

We use a hybrid cell to provide an antagonistic boundary condition. As shown in **Figure 1a**, a thin PDMS layer is coated on one ITO glass substrate to perform vertical alignment, while the other ITO glass substrate covered with photoalignment agent SD1 gives planar anchoring. They work together to generate a hybrid alignment for infiltrated LC 8CB (molecular structures of PDMS, SD1, and LC 8CB are revealed in Figure S1, Supporting Information). Here, all cell gaps are fixed at 8.6  $\mu\text{m}$  if

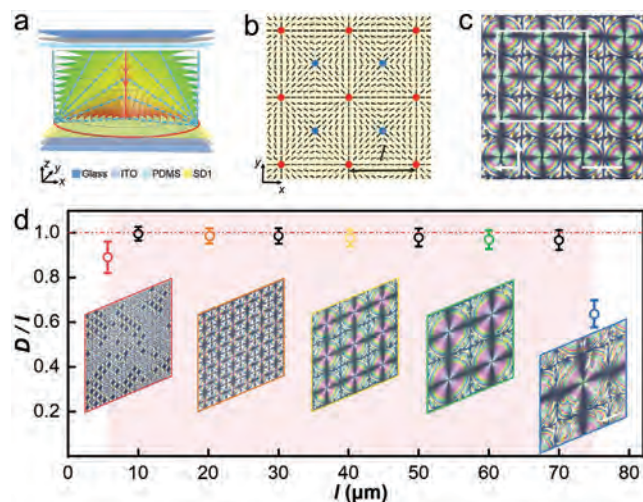


**Figure 1.** Alignment-guided TFCD array. a) 3D illustration of a TFCD formed in a hybrid cell. b) Radial alignment array with +1 (red dot) and -1 (blue dot) alignment singularities labeled in the planar alignment layer.  $l$  depicts the preset distance between adjacent singularities of the same species. c) Micrograph of the generated TFCD array when  $l = 30 \mu\text{m}$  under crossed polarizers. The white square corresponds to the alignment region in (b). d) Dependency of  $D/l$  on  $l$ . Insets show corresponding textures of  $l = 6, 20, 40, 60,$  and  $75 \mu\text{m}$ , respectively. The white arrows denote the directions of crossed polarizers. All scale bars indicate  $30 \mu\text{m}$ .

not specifically mentioned. In this case, TFCD is formed by parallel layers wrapped around a defect pair of a straight line and a circle (marked in red), and in each layer, rod-like LC molecules arrange parallel to the normal of layer planes.<sup>[24]</sup> According to the 3D configuration of the TFCD, the bottom director field is radial in the  $x$ - $y$  plane. That means a radial alignment matches the infinite rotational symmetry of a TFCD unit and thus facilitates its emergence.<sup>[25]</sup> Through delicately predesigning the alignments and corresponding singularities, the generation of TFCDs can be well regulated. As shown in Figure 1b, we set a tetragonal lattice of radial alignment regions. In the center of each unit, a +1 singularity (red dot) occurs, while a -1 singularity (blue dot) is formed where four adjacent radial alignments meet together. The distance between adjacent singularities of the same species is depicted by  $l$ . We utilize a multistep partly-overlapping photoalignment technique to record the designed information into the planar photoalignment layer.<sup>[26]</sup> The filled LC is cooled from isotropic phase (Iso) to SmA phase at a rate of  $1 \text{ }^\circ\text{C min}^{-1}$ , and then an ordered TFCD array is obtained. As shown in Figure 1c, TFCDs are addressed exactly by +1 singularities with diameter  $D$  equal to  $l$  when  $l = 30 \mu\text{m}$ . The uniform circular boundary and black Maltese cross in each unit verify the radial director distribution of the obtained TFCDs.

We systematically study the dependency of the domain size  $D$  on  $l$ . Figure 1d presents the relationship between  $D/l$  and  $l$ . When  $6 \mu\text{m} < l < 75 \mu\text{m}$ ,  $D/l \approx 1$ . It suggests that the domain size is strictly determined by  $l$ . In corresponding micrographs, the circular boundaries of units remain regular and uniform, and the centers of Maltese crosses are located exactly at the +1 singularities (Figure S2, Supporting Information). These phenomena indicate that the obtained TFCDs are precisely regulated by prealignment in this range of  $l$ . When  $l \leq 6 \mu\text{m}$ , the deviation of  $D/l$  increases. The limited alignment resolution hinders the formation of ideal radial anchoring, leading to the size nonuniformity under large layer curvatures. When  $l \geq 75 \mu\text{m}$ ,  $D/l$  drops to 0.65 suddenly. Additional FCDs emerge and severely truncate the central TFCD in each unit. Herein, the truncation results from the energetic relaxation in anchoring regions, which is nearly twice as large as the size of freely assembled TFCD.<sup>[20]</sup> The interference color variation among textures is caused by the slight variation of the director field among differently sized domains.

Since the locations of TFCDs are addressed by +1 singularities and domain sizes are exactly controlled by  $l$  in the range of  $\approx 6$ – $75 \mu\text{m}$ , both the domain size and lattice symmetry of TFCD are expected to be manipulated via properly preprogramming the planar photoalignment layer. **Figure 2** shows some complicated alignment patterns, by which alternate lines and square frames of two differently sized TFCDs ( $l = 20$  and  $40 \mu\text{m}$ , separately) and even hexagonal lattice are demonstrated. The ordered lattice and uniform domains verify that the formation of TFCDs faithfully follows the guidance of local alignment. In addition to the exhibited samples, more complicated TFCD arrays can be expected via preprogramming the photoalignment pattern. It releases the freedom of domain size and lattice symmetry and supplies a practical approach for free and faithful fabrication of TFCD arrays.

As mentioned above, the unique director distribution of TFCD enables a function of the microlens (**Figure 3a**).<sup>[15]</sup>

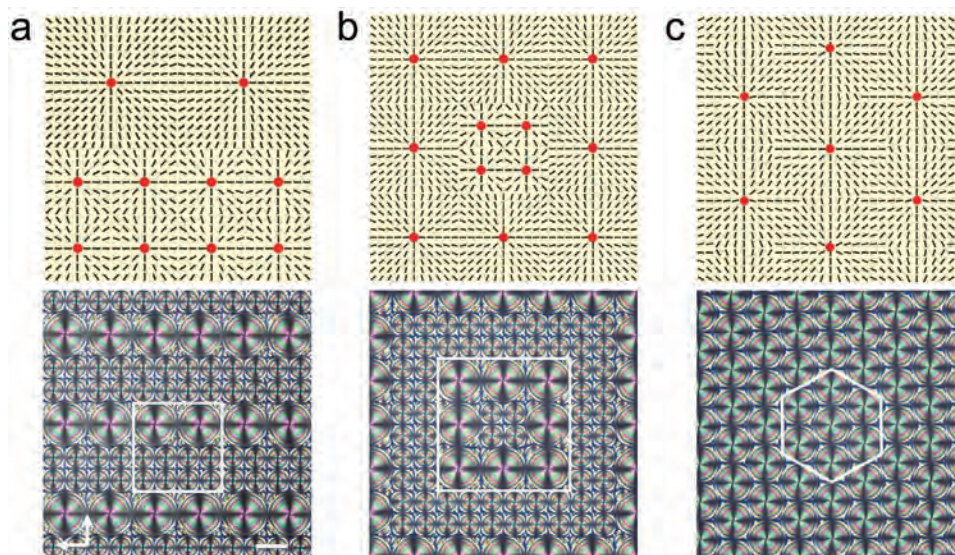


**Figure 2.** Domain size and lattice tailoring of TFCDs. The pre-designed alignment patterns and corresponding TFCDs of a) alternate lines, b) square frames of TFCDs with  $l = 20$  and  $40 \mu\text{m}$ , and c) hexagonal lattice of TFCDs with  $l = 30 \mu\text{m}$ . The white arrows denote the directions of crossed polarizers. The scale bar indicates  $30 \mu\text{m}$ .

Therefore, when a light beam passes through such a TFCD array, it is focused by the sample similar to an MLA. As shown in Figure 3b, an optical microscope is adopted to characterize the imaging performance of the MLA.<sup>[15a]</sup> We systematically study the influences of  $D$  and the film thickness  $h$  on the focal length  $f$  of the MLA (Figure 3c).  $f$  can be calculated as  $f = \frac{(D_n/2)^2}{2\Delta n h}$ , where  $D_n$  is the diameter of naturally grown

TFCDs, and  $\Delta n$  is the maximum refractive index change from the center to the edge, here roughly equals the birefringence of 8CB.<sup>[15a]</sup> It has been reported previously that  $D_n$  is proportional to  $h$ , thus giving rise to a linearly growing  $f$  along with  $D_n$  and  $h$ .<sup>[27]</sup> Herein,  $D$  is precisely defined by  $l$ , which is significantly smaller than  $D_n$ . The director distribution of the obtained TFCD is more like a central part of the naturally grown one with a slight difference in  $\Delta n$ . The increases of  $h$  and  $D$  flatten the phase profile separately and cause the enlargement of  $f$  (Figure 3c). When SmA phase is heated to N phase, the lamellar structure collapses, and the director distribution turns to the situation of a radially aligned hybrid nematic cell (Figure 3d). As a result, the imaging effect vanishes.

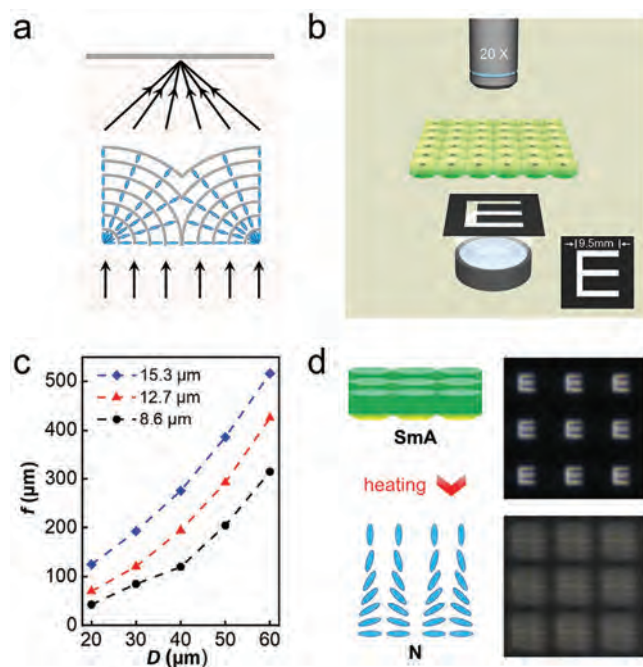


**Figure 3.** The imaging effect of TFCDs. a) Schematic diagram of the imaging effect for a single TFCD. b) Setup illustration for imaging. c) Dependencies of  $f$  on  $D$  of TFCDs with different  $h$ . d) Structure evolution and imaging performance for a sample in SmA phase and N phase, respectively.

Although the ordered configuration of TFCD permits an excellent focusing property, the robustness of the configuration hinders the tunability of the MLA. Moreover, the complicated configuration totally collapses when heated to N phase. Therefore, the challenge is to keep the director distribution of TFCD and possess the stimuli-responsiveness of N phase simultaneously. To solve this problem, we introduce a polymer stabilization strategy.<sup>[28]</sup> 2 wt% RM257 and 0.5 wt% photo-initializer are doped into the LC mixture of 8CB and 5CB (molecular structures of LC 5CB and RM257 are revealed in Figure S1, Supporting Information), which is the optimized ratio. When RM257 content increases over 3%, the formation of TFCDs will be affected, leading to irregular and frustrated TFCDs. It is attributed to the size difference among RM257 mesogen, 5CB, and 8CB, causing deformed smectic layers. On the contrary, when the content of RM257 is less than 1.5%, the TFCD-like director distribution cannot be stabilized well.

After TFCDs are generated, the cells are exposed to a UV LED for polymerization. As illustrated in Figure 4a, a polymer network is generated and helps to stabilize the director distribution of TFCD. Figure 4b presents the phase diagram of polymer-stabilized samples with different 5CB

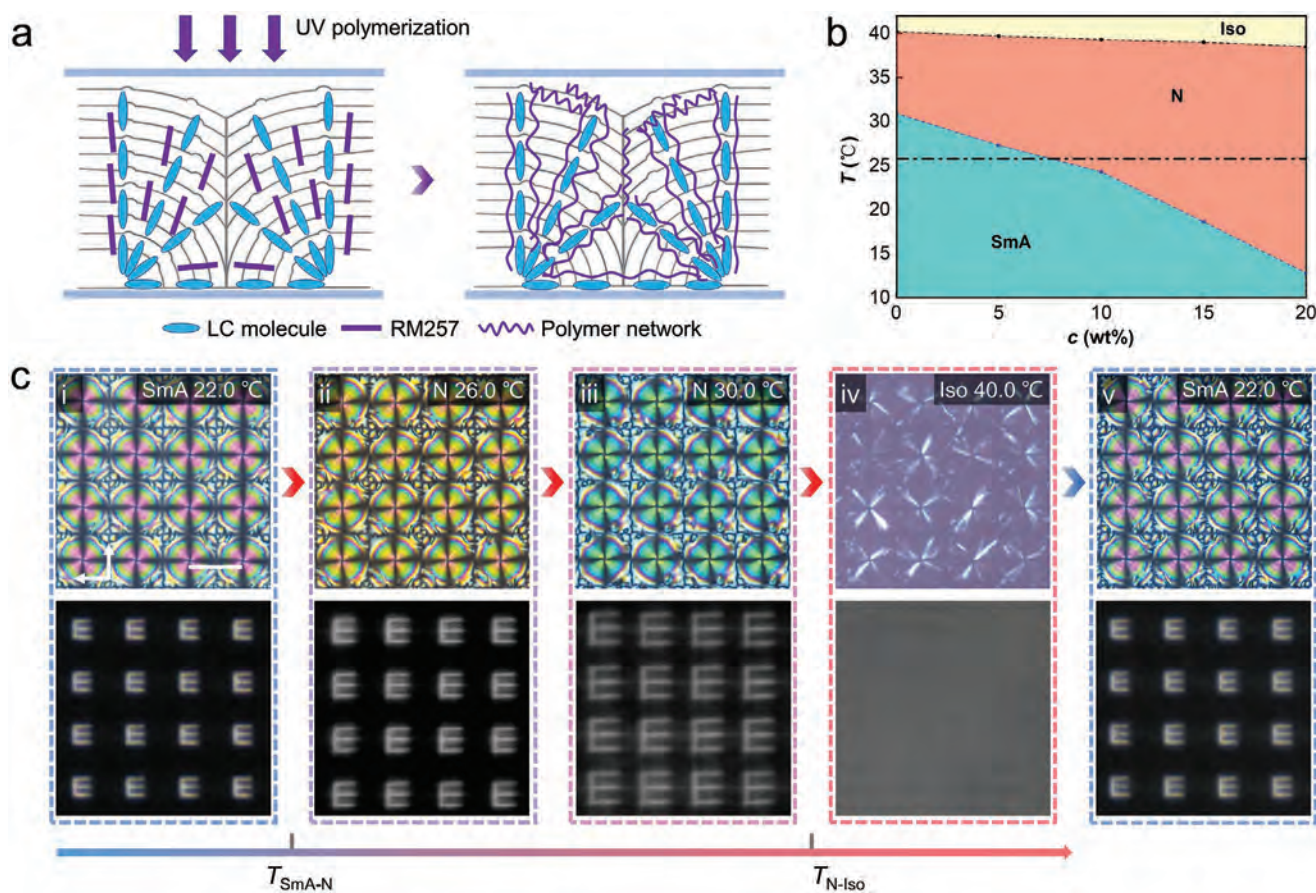


**Figure 4.** Polymer-stabilized TFCD array. a) Schematic illustration of the UV polymerization process. b) Phase diagram of polymer-stabilized samples with different 5CB concentrations  $c$ . c) Texture evolution of the polymer-stabilized TFCD array (top row) and corresponding imaging performance (bottom row) in a temperature cycle. Red and blue arrows represent heating and cooling processes, respectively. The white arrows denote the directions of crossed polarizers. The scale bar indicates 30  $\mu\text{m}$ .

concentrations  $c$ . The significant interference color change is used as the evidence for SmA-N phase transition, and the disappearance of the texture indicates the N-Iso phase transition (Figure S3, Supporting Information). The measured nematic ranges are  $\approx 30.9\text{--}40.2$  °C,  $\approx 27.3\text{--}39.7$  °C,  $\approx 24.3\text{--}39.3$  °C,  $\approx 18.6\text{--}39$  °C,  $\approx 12.8\text{--}38.5$  °C for samples of  $c = 0\%$ , 5%, 10%, 15% and 20%, respectively. Along with the increase of  $c$ , the SmA-N phase transition point decreases continuously, while the clearing point (N-Iso) nearly remains constant. When  $c$  exceeds 10 wt%, the mixture keeps N phase at room temperature. Here, we choose  $c = 10$  wt% as an example. When such a sample is heated, polymer-stabilized TFCDs are observed over the whole nematic range (Figure 4c-ii,iii), unlike the unpolymerized TFCDs that vanish after SmA-N phase transition (Figure S4, Supporting Information). During this process, a tetragonal TFCD lattice remains intact except for a continuous color variation due to the variation in  $\Delta n$ . The stabilized configuration is further verified by the imaging effect of the corresponding textures. It is demonstrated that  $\Delta n$  decreases with increasing  $T$ , until it disappears in the isotropic phase.<sup>[29]</sup> As mentioned above,  $f$  is inversely proportional to  $\Delta n$ . Thus, both  $f$  of the MLA and corresponding magnification of images increase along with  $T$  (Figure S5, Supporting Information and Figure 4c). As

temperature approaches the N-Iso phase transition point, the change of  $f$  becomes more dramatic, which is consistent with the  $\Delta n$  variation presented in ref. [29]. When the sample is cooled to SmA phase again, the TFCDs reappear at their initial location (Figure 4c-v). Moreover, the texture and imaging properties are almost unchanged compared to the initial state (Figure 4c-i) after tens of temperature cycles. This reveals the thermally reversible tunability of the polymer-stabilized TFCDs-based MLA.

In addition to the thermally induced birefringence variation, the electric field is considered a more convenient approach for the demonstration of tunability. For the polymer-stabilized TFCDs in SmA phase, they are still insensitive to the electric stimuli and cannot be recovered to the original texture very well when the voltage is removed (Figure S6, Supporting Information), just as the case for pure SmA 8CB (Figure S7, Supporting Information). By contrast, the electrical tunability is easily carried out in N phase. Thus, we systematically investigate the performance of the above MLA at room temperature (i.e., in N phase). When the electric field is vertically applied to the sample, the electric force enlarges the tilt angle of LC director, and drives it parallel to the substrate normal. It can be calculated by the electric coherence length  $\xi = (K/\epsilon_0\Delta\epsilon)^{1/2}/E$ ,

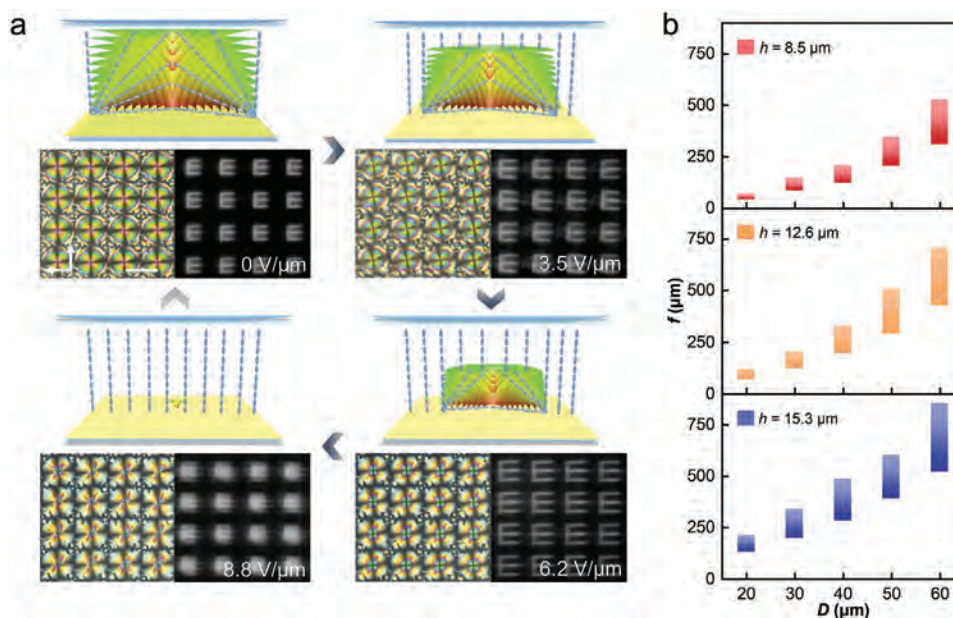


**Figure 5.** Electrically tuned  $f$  of the MLA. a) Director distributions (top row), texture variations of the MLA (bottom-left), and corresponding imaging performances (bottom-right) in a voltage cycle at room temperature. The white arrows denote the directions of crossed polarizers. The scale bar indicates 30  $\mu\text{m}$ . b) Dependency of the  $f$ -tuning range on  $D$  of MLAs with different  $h$ .

where  $K$  is the elastic constant of the LC,  $\epsilon_0$  is the permittivity of vacuum,  $\Delta\epsilon$  is the dielectric anisotropy and  $E$  is the electric field intensity.<sup>[11]</sup> Here, individual TFCDs are separated by flat and parallel smectic layers (i.e., homeotropic state),<sup>[24b]</sup> and the superstrate is vertically prealigned. Thus, the LC in these regions tends to be driven to a homeotropic state more easily. Along with the increasing of applied electric field  $E$ , both the size and thickness of TFCD-like domains decrease gradually, which is also verified by the experimental results.

Along with the increase of  $E$ ,  $D$  of TFCD-like textures reduces gradually, and  $\Delta n$  decreases toward zero accordingly.<sup>[30]</sup> As a result,  $f$  is dynamically tuned by  $E$ . **Figures 5a** vividly reveal the changes in domain size and image amplifications. The textures fade away when  $E > 8.8 \text{ V } \mu\text{m}^{-1}$ , and the imaging effect vanishes accordingly. With decrease of  $E$ , the same sequences of the TFCD-like textures and corresponding images reappear (Figure S8, Supporting Information). The textures and imaging functions are kept good for over several tens of voltage cycles. This shows that the  $f$ -tuning process is reversible by adjusting  $E$ . This result suggests that the polymer network remains stable during the electric-field-driven process. We also study the influence of  $D$  and  $h$  on the  $f$ -tuning range of the MLA. As shown in Figure 5b, the total tunable range reaches 810  $\mu\text{m}$ .

By presetting the locations and species of alignment singularities, the director distribution is locally guided by the anchoring when LC turns from Iso to N phase. After undergoing the N-SmA phase transition, a uniformly ordered TFCD array is obtained. This can be explained by a memory effect of director orientation during the N-SmA phase transition, which directs the deformation of smectic layers.<sup>[25,31]</sup> Thus through properly designing the radial alignment lattice, 3D layered structures of TFCDs including the domain size and lattice symmetry are freely manipulated. Photoalignment is a noncontact

technique that avoids mechanical damage and residual debris and is suitable for large-area and high-quality hierarchical architecting. In an opposite SmA-N phase transition process, the layered structures of TFCDs collapse. Fortunately, by means of polymer stabilization and composite optimization, the MLA with continuously electric-field-tunable focal length is demonstrated, which can be fully reversible with voltage over a wide range of temperatures. This is attributed to the presence of polymer network, which helps to anchor the LC orientation, and the effect is successfully maintained even after many heating or electric driving cycles. The response time of such MLA is in millisecond scale, comparable to the MLA fabricated by traditional polymer-stabilized nematic LCs.<sup>[32]</sup> The simple and low-cost strategy provides a practical route for manufacturing tunable MLAs. Considering the superiorities of flatness, miniaturization, integration, and tunability, such MLAs are expected to provide new opportunities for 3D display, optical interconnect, and bionics. Additionally, the polymer stabilization strategy can be further extended to other smectic configurations, such as oily streaks<sup>[33]</sup> and deformed FCDs.<sup>[34]</sup> This work widens our knowledge of self-organized configurations and explores the practical application of such TFCD-based MLA, which can also be extended to other optical scenarios.

### 3. Conclusion

We propose a strategy for tunable layered hierarchical structures with highly flexible configuration tailoring. Radial alignment lattices are specially preset to precisely manipulate the lattice symmetry and domain size of TFCDs. After polymer stabilization and composition optimization, the sample simultaneously keeps the TFCD-like director distribution and possesses

stimuli-responsiveness at room temperature. The stabilized hierarchical configuration is demonstrated as an MLA with reversible thermal and electrical tunability. This work is a vital step forward to expanding the knowledge of smectic hierarchical structures and may release many unanticipated advanced dynamic photonic applications.

## 4. Experimental Section

**Materials:** 8CB (HCCH, China) has a phase sequence of an Iso-N transition at 40.5 °C and an N-S transition at 33.5 °C. **Reactive monomer RM257 (HCCH, China) and photo initializer were dissolved in 8CB and 5CB (HCCH, China) LC mixtures at concentrations of 2 wt% and 0.5 wt%, respectively.** Then, the LC mixture was stirred at 65 °C for 1 h. The photoalignment agent SD1 (Dai-Nippon Ink and Chemicals, Japan) was dissolved in dimethylformamide at a concentration of 0.3 wt%. Polydimethylsiloxane (PDMS, Dow Corning, USA) was utilized as an alignment film for homeotropic anchoring.

**Sample Fabrication:** The glass substrates were successively treated by ultrasonic washing and UV-ozone cleaning. SD1 was spin-coated onto the substrates and cured at 100 °C for 10 min. Then, the substrate coated with SD1 layer was exposed under a dynamic polarization microlithography system to carry out the desired planar anchoring patterns. A thin film of PDMS was spin-coated onto the other substrate and baked at 120 °C for 20 min. Subsequently, two pieces of substrate were separated by UV glue doped with spacers to form a hybrid cell. The 8CB and LC mixtures were then capillary-filled into cells at 65 °C and then annealed to N and S states successively with a heating stage (Linkam LTS 120, UK). Cells were exposed to a UV LED (365 nm, 132 μW cm<sup>-2</sup>) for 5 min to polymerize the TFCDs.

**Characterization:** Micrographs were captured on a polarized optical microscope (Nikon 50i, Japan) with a pair of crossed polarizers and recorded by a CCD camera (Nikon DS-Ri1, Japan). A 1 kHz square wave AC voltage generated by a function generator (Agilent Technologies Inc. 33522B, USA) and subsequently amplified by a voltage amplifier (TEGAM 2340, USA) was applied to the cells to drive the LCs.

## Supporting Information

Supporting Information is available from the Wiley Online Library or from the author.

## Acknowledgements

J.-B.W. and S.-B.W. contributed equally to this work. The authors thank De-Wei Zhang for his constructive discussions. This work was sponsored by the National Natural Science Foundation of China (NSFC) (62035008 and 61922038), the Natural Science Foundation of Jiangsu Province, Major Project (BK20212004), and the Fundamental Research Funds for the Central Universities (021314380189).

## Conflict of Interest

The authors declare no conflict of interest.

## Data Availability Statement

The data that support the findings of this study are available from the corresponding author upon reasonable request.

## Keywords

alignment lattices, electrical tunability, hierarchical architectures, liquid crystals, polymer stabilization

Received: May 30, 2022

Published online:

- [1] D. K. Yang, S. T. Wu, *Fundamentals of Liquid Crystal Devices*, Wiley, New York **2014**.
- [2] Y. J. Zhou, Y. D. Yuan, T. B. Zeng, X. R. Wang, D. L. Tang, F. Fan, S. C. Wen, *Opt. Lett.* **2020**, *45*, 5716.
- [3] a) L. L. Tian, F. Chu, W. X. Zhao, L. Li, Q. H. Wang, *Opt. Lett.* **2021**, *46*, 5870; b) M. Jiang, Y. B. Guo, H. Yu, Z. Y. Zhou, T. Turiv, O. D. Lavrentovich, Q. H. Wei, *Adv. Mater.* **2019**, *31*, 1808028.
- [4] Z. Q. He, K. Yin, S. T. Wu, *Light: Sci. Appl.* **2021**, *10*, 134.
- [5] a) A. Honglawan, S. Yang, *Nanoscience with Liquid Crystals: From Self-Organized Nanostructures to Applications*, Springer, Cham **2014**; b) Z. G. Zheng, Y. Li, H. K. Bisoyi, L. Wang, T. J. Bunning, Q. Li, *Nature* **2016**, *531*, 352.
- [6] a) J. Kobashi, H. Yoshida, M. Ozaki, *Nat. Photonics* **2016**, *10*, 389; b) M. Rafayelyan, G. Tkachenko, E. Brasselet, *Phys. Rev. Lett.* **2016**, *116*, 253902; c) P. Chen, L. L. Ma, W. Hu, Z. X. Shen, H. K. Bisoyi, S. B. Wu, S. J. Ge, Q. Li, Y. Q. Lu, *Nat. Commun.* **2019**, *10*, 2518.
- [7] S. Y. Cho, M. Takahashi, J. Fukuda, H. Yoshida, M. Ozaki, *Commun. Mater.* **2021**, *2*, 39.
- [8] K. X. Chen, C. T. Xu, Z. Zhou, Z. L. Li, P. Chen, G. X. Zheng, W. Hu, Y. Q. Lu, *Laser Photonics Rev.* **2022**, *16*, 2100591.
- [9] H. Y. D. Sigaki, E. K. Lenzi, R. S. Zola, M. Perc, H. V. Ribeiro, *Sci. Rep.* **2020**, *10*, 7664.
- [10] J. H. Xiong, E. L. Hsiang, Z. Q. He, T. Zhan, S. T. Wu, *Light: Sci. Appl.* **2021**, *10*, 216.
- [11] P. G. de Gennes, J. Prost, *The Physics of Liquid Crystals*, Oxford University Press, Oxford **1993**.
- [12] a) J. B. Fournier, I. I. Dozov, G. Durand, *Phys. Rev. A* **1990**, *41*, 2252; b) Y. H. Kim, D. K. Yoon, H. S. Jeong, O. D. Lavrentovich, H. T. Jung, *Adv. Funct. Mater.* **2011**, *21*, 610.
- [13] a) Y. H. Kim, D. K. Yoon, H. S. Jeong, J. H. Kim, E. K. Yoon, H. T. Jung, *Adv. Funct. Mater.* **2009**, *19*, 3008; b) D. S. Kim, Y. J. Cha, H. Kim, M. H. Kim, Y. H. Kim, D. K. Yoon, *RSC Adv.* **2014**, *4*, 26946.
- [14] a) D. K. Yoon, M. C. Choi, Y. H. Kim, M. W. Kim, O. D. Lavrentovich, H. T. Jung, *Nat. Mater.* **2007**, *6*, 866; b) D. S. Kim, A. Honglawan, S. Yang, D. K. Yoon, *ACS Appl. Mater. Interfaces* **2017**, *9*, 7787.
- [15] a) L. L. Ma, S. B. Wu, W. Hu, C. Liu, P. Chen, H. Qian, Y. Wang, L. Chi, Y. Q. Lu, *ACS Nano* **2019**, *13*, 13709; b) Y. H. Kim, J. O. Lee, H. S. Jeong, J. H. Kim, E. K. Yoon, D. K. Yoon, J. B. Yoon, H. T. Jung, *Adv. Mater.* **2010**, *22*, 2416; c) Y. H. Kim, H. S. Jeong, J. H. Kim, E. K. Yoon, D. K. Yoon, H. T. Jung, *J. Mater. Chem.* **2010**, *20*, 6557.
- [16] a) M. C. Choi, T. Pfohl, Z. Y. Wen, Y. L. Li, M. W. Kim, J. N. Israelachvili, C. R. Safinya, *Proc. Natl. Acad. Sci. U. S. A.* **2004**, *101*, 17340; b) A. Honglawan, D. A. Beller, M. Cavallaro, R. D. Kamien, K. J. Stebe, S. Yang, *Adv. Mater.* **2011**, *23*, 5519.
- [17] J. P. Bramble, S. D. Evans, J. R. Henderson, T. J. Atherton, N. J. Smith, *Liq. Cryst.* **2007**, *34*, 1137.
- [18] J. M. Ok, Y. H. Kim, H. S. Jeong, H. W. Yoo, J. H. Kim, M. Srinivasarao, H. T. Jung, *Soft Matter* **2013**, *9*, 10135.
- [19] J. M. Ok, Y. H. Kim, T. Y. Lee, H. W. Yoo, K. Kwon, W. B. Jung, S. H. Kim, H. T. Jung, *Langmuir* **2016**, *32*, 13418.
- [20] L. L. Ma, M. J. Tang, W. Hu, Z. Q. Cui, S. J. Ge, P. Chen, L. J. Chen, H. Qian, L. F. Chi, Y. Q. Lu, *Adv. Mater.* **2017**, *29*, 1606671.
- [21] S. B. Wu, L. L. Ma, P. Chen, H. M. Cao, S. J. Ge, R. Yuan, W. Hu, Y. Q. Lu, *Adv. Opt. Mater.* **2020**, *8*, 2000593.

- [22] S. B. Wu, H. M. Cao, J. B. Wu, L. L. Ma, Y. Q. Lu, W. Hu, *Adv. Opt. Mater.* **2022**, *10*, 2102754.
- [23] A. Suh, H. Ahn, T. J. Shinc, D. K. Yoon, *J. Mater. Chem. C* **2019**, *7*, 1713.
- [24] a) M. Kleman, O. D. Lavrentovich, *Liq. Cryst.* **2009**, *36*, 1085; b) M. Kleman, O. D. Lavrentovich, *Phys. Rev. E* **2000**, *61*, 1574.
- [25] a) M. J. Gim, D. A. Beller, D. K. Yoon, *Nat. Commun.* **2017**, *8*, 15453; b) A. Suh, M. J. Gim, D. Beller, D. K. Yoon, *Soft Matter* **2019**, *15*, 5835.
- [26] P. Chen, S. J. Ge, W. Duan, B. Y. Wei, G. X. Cui, W. Hu, Y. Q. Lu, *ACS Photonics* **2017**, *4*, 1333.
- [27] F. Serra, M. A. Gharbi, Y. Luo, I. B. Liu, N. D. Bade, R. D. Kamien, S. Yang, K. J. Stebe, *Adv. Opt. Mater.* **2015**, *3*, 1287.
- [28] a) H. Kikuchi, M. Yokota, Y. Hisakado, H. Yang, T. Kajiyama, *Nat. Mater.* **2002**, *1*, 64; b) M. Wang, C. Zou, J. Sun, L. Y. Zhang, L. Wang, J. M. Xiao, F. S. Li, P. Song, H. Yang, *Adv. Funct. Mater.* **2017**, *27*, 1702261; c) S. M. Ye, Y. X. Teng, A. Juan, J. Wei, L. Y. Wang, J. B. Guo, *Adv. Opt. Mater.* **2017**, *5*, 1600956.
- [29] A. Nesrullajev, *J. Mol. Liq.* **2022**, *345*, 117716.
- [30] H. Ren, S. T. Wu, *Appl. Phys. Lett.* **2003**, *82*, 22.
- [31] S. M. Hare, P. B. Lunsford, M. Kim, F. Serra, *Materials* **2020**, *13*, 3761.
- [32] H. C. Lin, Y. H. Lin, *Appl. Phys. Lett.* **2011**, *98*, 083503.
- [33] a) I. Gharbi, A. Missaoui, D. Demaille, E. Lacaze, C. Rosenblatt, *Crystals* **2017**, *7*, 358; b) G. Babakhanova, J. Krieger, B. X. Li, T. Turiv, M. H. Kim, O. D. Lavrentovich, *J. Biomed. Mater. Res., Part A* **2020**, *108*, 1223.
- [34] G. Boniello, V. Vilchez, E. Garre, F. Mondiot, *Macromol. Rapid Commun.* **2021**, *42*, 2100087.